Mobile Terahertz Inter-Small-Satellite Links with Angular Dispersion

Keerthi Dasala
Elmore Family School of Electrical and Computer Engineering, Purdue University, West Lafayette, IN, USA

***Abstract*—Terahertz (THz) inter-satellite links (ISLs) enable high-data-rate communication between satellites, addressing the need for faster communication in modern satellite systems. While more resilient than RF and optical systems, THz ISLs are still vulnerable to orbital perturbations, leading to severe beam misalignment and signal degradation. This paper presents the a first study evaluating composite directional THz links to mitigate the impact of these perturbations on THz ISLs. We leverage the angular dispersion property arising from wideband frequency diversity of THz channels and employ THz-scale Leaky Wave Antennas (LWAs) for passive beam steering, enhancing spatial coverage and adapting to satellite position changes. Through model-driven evaluations and over-the-air measurements, we quantify the perturbation tolerance of lab-scale LWA-based links across various geometries, highlighting bandwidth expansion limitations in mitigating angular instability and optimizing LWA geometry for reliable, high-performance THz ISLs.**

I. Introduction

The growing demand for faster, more reliable networks to support emerging verticals like industrial automation, autonomous vehicles, and smart cities is pushing conventional terrestrial networks to their limits. The future of communication extends beyond the ground, encompassing aerial and space-based communication systems to form a seamless global network. In this context, the *Internet of Space Things (IoST)* envisions CubeSats (or nanosatellites) forming a space-based network to enable seamless, ubiquitous data transfer, with throughput reaching multi-hundred gigabits-per-second (Gbps) [1]. In this landscape, inter-satellite links (ISLs) are crucial for connecting small satellite constellations and enabling high-speed data transmission between space, aerial, and terrestrial networks as illustrated in Fig. 1.

Current satellite communication systems rely on microwave frequency bands L-band (1–2 GHz), Ka-band (26.5–40 GHz), and V-band (40–75 GHz) and optical laser links. While these bands have effectively served many missions, they face growing challenges: *(i) Bandwidth constraints:* While microwave bands are robust, they offer limited spectral resources, creating bottlenecks for high-throughput ISLs, particularly in dense constellations like low Earth orbit (LEO) [2] and require large antennas to achieve high gain—conflicting with the size, weight, and power (SWaP) constraints of small satellites *(ii) Alignment sensitivity:* Satellites experience orbital perturbations from gravitational forces, solar radiation pressure, and atmospheric drag, causing beam misalignment. This is especially challenging for highly directional optical and high-frequency RF links, which require constant realignment in dynamic orbital environments [3]. *(iii) Interference and attenuation:*

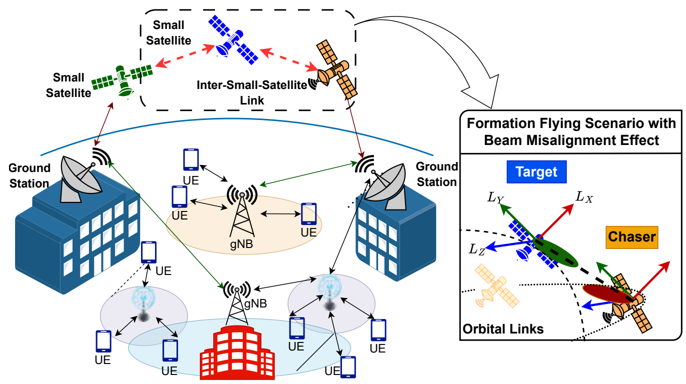

Fig. 1: Illustration of next-generation terrestrial networks enabled by inter-satellite links (formation flying scenario is enlarged to show the beam misalignment effect).

Congestion in lower RF bands can hinder high-throughput ISLs, while atmospheric effects and line-of-sight blockages affect both microwave and optical systems. The THz band offers a promising supplement—not necessarily a panacea—to existing ISL solutions. THz frequencies can support ultra-high data rates and compact antennas, which is advantageous for small satellites. However, THz links are still subject to line-of-sight requirements, atmospheric attenuation, and beam-pointing issues, indicating that robust beam management is crucial for harnessing the THz band's full potential.

In this paper, we present the first experimental study and performance evaluation of THz ISLs to address the effects of beam misalignment caused by orbital perturbations. We make the following contributions. First, we explore how the composite multi-channel, frequency-diverse THz channels can be utilized to realize high-directional, high-bandwidth THz ISLs. With the large bandwidth available in the THz regime, directional transmission exhibits angular dispersion, meaning the radiation direction varies with each frequency component in the band. Instead of requiring real-time mechanical or electronic beam steering, this property, by extension, can naturally widen the spatial signal footprint as bandwidth increases. While prior studies have explored angular dispersion to enhance wireless network performance [4]–[6], we propose that this frequency-dependent radiation offers significant advantages for maintaining robustness and spatial coverage in THz ISLs, allowing for rapid beam steering to accommodate satellite positions shifts due to external disturbances.

ISBN 978-3-903176-73-7 © 2025 IFIP

Second, to study the performance of THz ISLs with frequency-varying radiation, we employ a promising THz-scale directional Leaky Wave Antenna (LWA) that features the highest angular dispersion and frequency-agile beam steering capability to date [5], [7], [8]. While LWAs have been studied in millimeter-wave or near-THz regimes [4], their viability for long-range, space-based links has not been thoroughly explored. Indeed, a moving satellite at a lower angle relative to the LWA accesses higher frequencies more effectively than lower frequencies and vice versa, resulting in angle-dependent and non-uniform rates across the transmission band. To establish the working principles of a wideband THz LWA-based ISL, we develop a physics-based analytical model to evaluate the ISL link's capability for misalignment mitigation across continuously varying link geometries and use it to characterize the achievable SNR and data rate.

Finally, we perform the first experimental emulation of angularly dispersive THz ISLs using over-the-air measurements of a wideband THz transmission from a custom-built LWA. Using a mix of model-based predictions and over-the-air experiments in a benchtop environment, we first quantify and assess the perturbation tolerance of LWA-based THz ISLs, focusing on the effects of dynamic beam steering, misalignment tolerance, and achievable data rates. Although our setup does not replicate full orbital distances (which require addressing power amplification, free-space loss, and extreme temperature variations), it rigorously characterizes fundamental parameters—beam width, coverage, frequency-dependent gain—that must be scaled for real deployments. Our findings reveal that LWA-based ISLs tolerate misalignments within $-10°$ to $10°$, ensuring robust communication across various geometries. We then analyze the influence of bandwidth expansion on tolerance and throughput, highlighting that while wider bandwidth provides a broader spatial-signal footprint that can enhance tolerance, the improvement in perturbation tolerance does not predictively scale proportionally with bandwidth expansion. We also investigate how LWA geometry impacts link performance and highlight that by adjusting the attenuation coefficient and plate separation results in a broader, more directional beam, enabling stable, high-performance transmission links.

II. Primer: Inter-Small-Satellite Links

Small satellites, with their smaller size, weight, and power compared to traditional low Earth orbit (LEO), medium Earth orbit (MEO), and geosynchronous equatorial orbit (GEO) satellites, offer shorter development cycles and lower costs. Their compact design and use of off-the-shelf components [9] have led to increased satellite formation flying missions, where multiple satellites work closely together for tasks like remote sensing and data exchange. Reliable, low-latency communication is crucial for these missions, especially as more explore the solar system and beyond [10]. ISLs are thus vital for both near-Earth and deep-space communications.

Orbital Perturbation in Small Satellites. Establishing satellite connections requires precise beam pointing, which can be

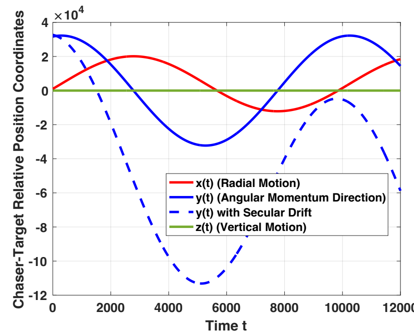

(a)

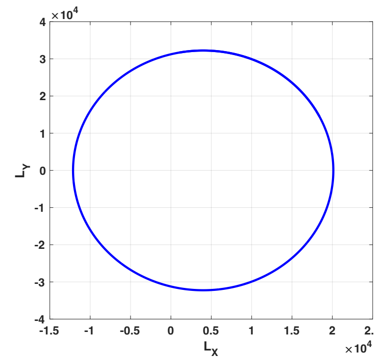

(b)

Fig. 2: (a) Chaser coordinates in LVLH frame and (b) Chaser motion as seen from L_Z axis.

disrupted by orbital dynamics, leading to misaligned beams and degraded communication. Key factors include Earth's oblateness (J2 Effect), solar radiation pressure, and gravitational forces from the Moon, Sun, and other celestial bodies, which cause gradual shifts in a satellite's orbital plane and require occasional adjustments for alignment.

When a pair of satellites (denoted as a target and a chaser for differentiation) located in the same/ different circular orbit with a relatively small distance, the relative motion of the chaser with respect to the target under general perturbations can be expressed using the Clohessy-Wiltshire Equations [11], and these equations are based on local-vertical-local-horizontal (LVLH) frame, shown as vectors in Fig. 1 and expressed as

$$\ddot{x} - 3n^2x - 2n\dot{y} = 0 \tag{1a}$$

$$\ddot{y} + 2n\dot{x} = 0 \tag{1b}$$

$$\ddot{z} + n^2z = 0 \tag{1c}$$

In the LVLH frame, the x-axis points along the radius vector, the y-axis follows the angular momentum vector, and the z-axis represents vertical motion out of the orbital plane. The accelerations $\ddot{x}$, $\ddot{y}$, and $\ddot{z}$ correspond to local directions, while velocities ($\dot{y}$, $\dot{z}$) and positions (y, z) represent motion relative to the target. A closed-form solution for the chaser's relative position over time as detailed in prior works [9], [12] as:

$$x(t) = \frac{\dot{x}_0}{n} sin(nt) - \left(3x_0 + 2\frac{\dot{y}_0}{n} cos(nt)\right) + \left(4\dot{x}_0 + 2\frac{\dot{y}_0}{n}\right) \tag{2a}$$

$$y(t) = \left(6\dot{x}_0 + \frac{\dot{y}_0}{n}\right) sin(nt) + 2\frac{\dot{x}_0}{n} cos(nt) - (6nx_0 + 3\dot{y})\, t + \left(y_0 - 2\frac{\dot{x}_0}{n}\right) \tag{2b}$$

$$z(t) = z_0 cos(nt) + \frac{\dot{z}_0}{n} sin(nt) \tag{2c}$$

where $n = \sqrt{\mu/a^3}$ is the orbit velocity, μ is the standard gravitational parameter ($\mu \approx 3.98 \times 10^14\ m^3/s^2$ for Earth), and a is the orbital radius. Figure 2a shows the time evolution of the chaser's relative position coordinates $x(t)$, $y(t)$, and $z(t)$. The $x(t)$ coordinate oscillates sinusoidally over time, driven by the initial radial velocity $\dot{x}_0$, representing periodic motion toward and away from the target along the radial direction without long-term drift. In contrast, $y(t)$ experiences a secular drift due to the term $-(6nx_0 + 3\dot{y}_0)\, t$, causing the chaser to gradually move away from the target along the angular momentum direction, as shown in Fig. 2a. The $z(t)$ coordinate, representing vertical motion perpendicular to the orbital plane, remains bounded and periodic. As shown in Fig. 2b, the chaser's in-plane motion along the L_X and L_Y axes exhibits both periodic oscillations and secular drift, while its motion in the vertical direction stays periodic and stable despite orbital dynamics.

III. THz Inter-Small-Satellite Links

The Terahertz (THz) band (0.1-10 THz), positioned between microwave and optical frequencies, offers multi-GHz bandwidth and ultra-high data rates, making it ideal for satellite communications. We address the impact of orbital disturbances on THz ISL communications by using composite directional THz links that exploit multiple frequency channels and large bandwidths [13], [14]. These links introduce angular dispersion, where the beam direction varies with frequency, creating an angular spread that increases with bandwidth [5], [7]. This frequency-dependent radiation widens the signal footprint and spatial coverage, allowing the system to accommodate satellite position changes and enabling rapid beam steering in response to orbital dynamics. While this property has been considered for future THz networks [4], its potential for ISLs is underexplored. Here, we propose using a Leaky Wave Antenna (LWA) (see Fig. 3) to address continuous satellite misalignment in THz ISLs. LWAs exhibit strong frequency-dependent angular dispersion [4], [5], allowing passive beam steering simply by adjusting signal frequency without the need for mechanical steering. This wideband steerability enables continuous scanning across a range of angles, effectively compensating for satellite orientation shifts caused by orbital perturbations. Their ability to generate wider beams than traditional directional antennas also increases tolerance to minor misalignments, ensuring stable links.

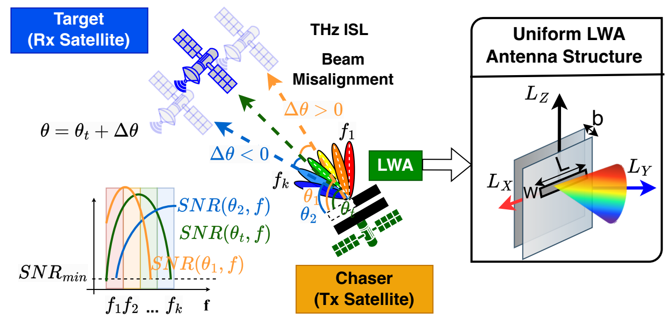

Fig. 3: Schematic of an LWA-based THz ISL maintaining wideband beam alignment. The LWA is along the L_X axis, with the L_Y axis perpendicular to the XY motion plane.

A. THz LWA-based ISL Characterization

Here, we present the characterization of THz LWA-based ISLs. To understand how this link achieves misalignment mitigation, we first discuss the fundamental principles of LWA.

LWA-based Spatial Filtering. An LWA consists of two parallel metal plates with a separation between them, where one of the plates features a slot that allows the guided wave to "leak" into free space, depicted in Fig. 3. By modeling the LWA as a finite-length slot that generates a diffraction pattern in the far-field, the radiation pattern is given by [5], [7], [15]

$$G(\theta, f) \propto sinc[(\beta(f) - j\alpha - k_0 cos\theta)\frac{L}{2}] \tag{3}$$

where θ, f, L, and k_0 represent the emission angle, frequency, the length of the slot, and the free-space wavenumber, respectively. $\beta(f)$ is the frequency-dependent propagation constant of the guided waves, and α describes the energy loss before leakage. We denote $D(\theta, f) = \frac{|G(\theta,f)|^2}{\frac{1}{\pi}\int_0^{\pi} |G(\theta',f)|^2 d\theta'}$ as the directivity gain in a given direction θ. According to the radiation pattern in Eqn. (3), the energy of a broadband signal radiates towards a specific emission angle, with varying radiated intensity due to the coupling between frequency and angle.

Scanning Angle with Frequency or Bandwidth. The angle at which a given frequency is maximally coupled in or out of the LWA can be found by maximizing $\text{Re}\{G(\theta, f)\}$, which yields

$$\theta_{max}(f) = sin^{-1}(\frac{c}{2bf}) \tag{4}$$

i.e., higher frequencies radiate maximally towards lower angles in an inverse and non-linear manner governed directly by the waveguide's geometry. Conversely, for a finite slot length, a wide range of frequencies radiate towards a particular emission angle, where the spectral peak and spectral bandwidth per radian for a receiver in the antenna's far field at a given angle, respectively, are given by [4]

$$f_{max}(\phi) = \frac{c}{2b\, sin\theta} \tag{5}$$

$$BW(\theta) = \frac{c}{2b \sin\theta \tan\theta} \tag{6}$$

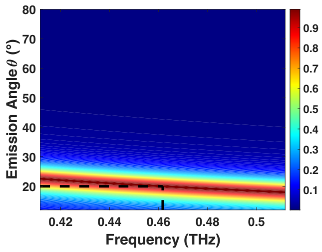

(a) $\theta_t = 20°$

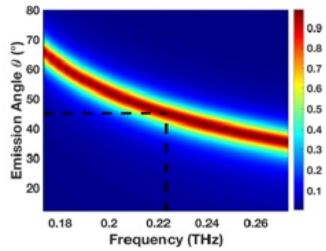

(b) $\theta_t = 45°$

Fig. 4: Model-based LWA radiation pattern for Rx satellite located at angles of 20° and 45° relative to Tx satellite.

The above LWA characterization has also been experimentally validated in prior work [5], [6], [16], [17].

In THz ISLs, the chaser (Tx) satellite uses an LWA to maintain communication with the target (Rx) satellite, a broadband detector. We denote θ_t as the emission angle pointing toward the target satellite, and orbital perturbations alter the relative angular location between satellites, leading to beam misalignment, represented as $\Delta\theta$. The LWA-based ISL, utilizing wideband frequencies, enables a rapid, passive response to the new target satellite position $\theta = \theta_t + \Delta\theta$, as shown in Fig. 3. The total bandwidth W is divided into K subchannels, each with equal bandwidth centered at f_k. Within the designated bandwidth, the radiation pattern varies with emission angles owing to the LWA's frequency-angle coupling.

Figure 4 showcases a 100 GHz bandwidth centered on f_{max} for $\theta_t = 20°$ and $\theta_t = 45°$, where maximum power is radiated at the center frequency. When a perturbation occurs, the radiation pattern shifts with $\Delta\theta$, radiating more power at lower frequencies for $\Delta\theta > 0$ and the reverse for $\Delta\theta < 0$. This demonstrates the LWA-based ISL's potential to adapt to orbital dynamics. Notably, $\theta_t = 45°$ covers a broader range of θ compared to $\theta_t = 20°$, indicating that higher emission angles accommodate severe perturbations and provide better tolerance to misalignment. However, with extreme perturbations and thus pronounced misalignment, the bandwidth with significant radiated power becomes more limited, indicating limited tolerance.

The radiation pattern affects the power received at the target satellite, which directly impacts the SNR. We model the SNR on the frequency subchannel f_k as

$$SNR(\theta, f_k) = \frac{P_t D(\theta, f_k)(\frac{c}{4\pi d f_k})^2}{N_0 W} \tag{7}$$

where P_t, d, and $\left(\frac{c}{4\pi d f_k}\right)^2$ are the transmit power, satellite distance, and free-space path loss, with the denominator representing noise power. The data rate is then calculated using the Shannon-Hartley Theorem:

$$R(\theta) = \sum_k W \times \log_2[1 + SNR(\theta, f_k)] \tag{8}$$

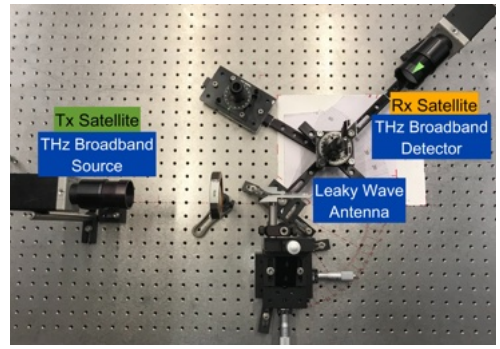

(a)

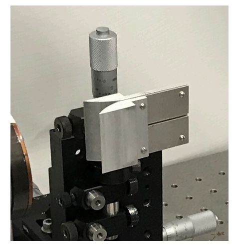

(b)

Fig. 5: (a) Setup of Experiment and (b) Custom-built LWA

IV. Evaluation & Performance Analysis

A. Experimental Testbed and Over-the-air Measurements

Studying actual THz ISLs is currently infeasible due to hardware limitations and the challenges involved in replicating orbital dynamics in a lab. Therefore, we employ a small-scale model to simulate continuous variations in link geometry caused by satellite movement, enabling us to evaluate the LWA's ability to mitigate beam misalignment. Although scaled down, this is the first experimental demonstration that offers key insights into the practical challenges and solutions for implementing THz ISLs. For experimental validation, we employ a custom $4.2cm \times 4.2cm$ parallel-plate LWA device at the transmitter, with each plate having a thickness of 0.9 mm thickness, a separation of 1 mm between them, and featuring a 3 cm long, 1 mm wide slot for waveguide emission, depicted in Fig. 5b. The radiation pattern is measured with the T-Ray 5600 THz time-domain spectroscopy (TDS) system [18], generating a wideband THz signal from 0.15 to 5 THz and returning a time-domain signal at a 33.3 THz sampling rate, which is followed by a discrete Fourier Transform to obtain the frequency spectrum with a resolution of 1.56 GHz. The THz pulse is focused onto the LWA using a lens, causing different frequency components to emit at varying angles.

Figure 5a shows our experimental setup, where the Tx satellite/broadband source and LWA are mounted on a rotating arm to vary LOS and orientations. Due to our THz source's limited power (sub-μW transmit power over the entire band), the transmission distance is constrained to the cm scale ($d = 43\ cm$). Atmospheric effects, such as attenuation or interference, are negligible at this scale, making the setup representative of

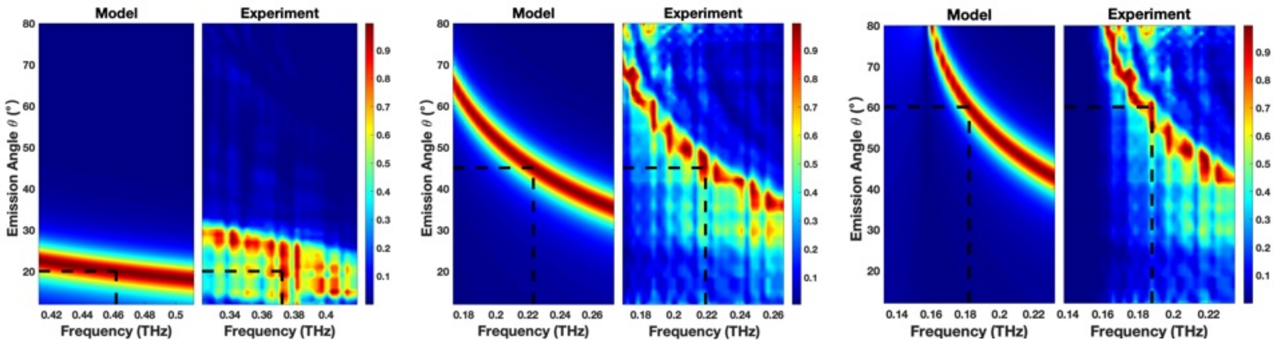

(a) $\theta_t = 20°$, BW = 100GHz (b) $\theta_t = 45°$, BW = 100GHz (c) $\theta_t = 70°$, BW = 100GHz

Fig. 6: Comparison between experimental and model-based radiation patterns and received SNR for different θ_t.

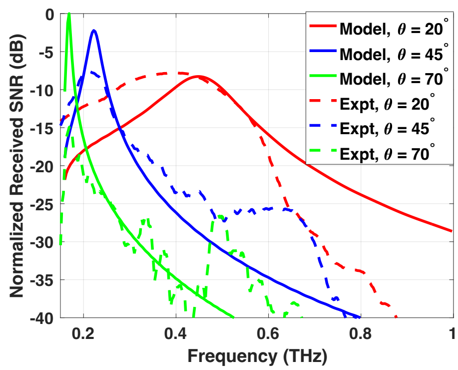

Fig. 7: Received SNR within the total bandwidth

satellite-to-satellite links, where similar conditions exist in the absence of atmospheric disturbances. To simulate the dynamic nature of the THz ISL under orbital perturbations, we place the broadband detector/ Rx satellite at various angles between $1° < \theta < 90°$ with a $0.5°$ resolution.

B. Foundational Differences between Experimental Link and Model Prediction

Imperfect model predictions and unavoidable experiment errors necessitate a thorough analysis of both theoretical model and experimental results. To develop a comprehensive understanding of the LWA-based THz ISL, we first examine the differences and similarities between the two links, specifically focusing on the radiation pattern (Eqn. (3)) and SNR distribution(Eqn. (7)).

Figures 6a, 6b and 6c compare the experimental and model-predicted radiation patterns at target angles, $\theta_t = 20°$, $\theta_t = 45°$ and $\theta_t = 70°$ respectively, over a 100 GHz bandwidth centered around the peak frequency f_{max}. At $\theta_t = 20°$, the experimental patterns shift toward lower frequencies compared to the model, potentially due to measurement inaccuracies where signal levels are weakened by higher frequency attenuation. By contrast, at $\theta_t = 45°$, the experimental and model-predicted patterns align more closely, indicating that the model captures the dominant angular-dispersive effects well at mid-range angles. At $\theta_t = 70°$, both the model and experiment exhibit broader angular coverage, as also suggested by the analysis in Sec. III; however, the experimental results show slightly more vertical spread in the high-power (green-to-red) region, implying a higher degree of misalignment tolerance in practice. Overall, these observations suggest that while the analytical model provides a reasonable baseline for angular dispersion at varying angles, real-world measurements can reveal additional nuances—particularly at lower angles and at the upper end of the angular range.

Figure 7 shows that SNR at lower emission angles exhibits a flatter distribution, while higher emission angles have a more peaked distribution. The spectral peak at $\theta = 45°$ is closer to $\theta = 70°$ than $\theta = 20°$, supporting earlier findings that a broader angular range is covered at higher emission angles. While the model predicts a higher peak SNR at $\theta = 70°$, the experiment shows an opposite trend, with $\theta = 70°$ yielding a lower peak SNR than $\theta = 20°$—over 10 dB lower than predicted by the model. Additionally, at lower emission angles like $\theta = 20°$, the model underestimates the SNR, suggesting the received power is higher than predicted. These discrepancies can be attributed to beam asymmetry and non-monotonic irregularities in measured beam pattern differently impacting the spatial-spectral profile of the Rx, which is not fully captured by the model. Furthermore, deviations between the model and experiment, particularly at higher frequencies and lower power levels, likely arise from experimental errors and idealizations in model (such as assuming infinitesimal plate thickness and perfect coupling efficiency), becoming more pronounced as frequency increases.

C. Perturbation Tolerance Analysis

1) Quantization of Tolerance to Misalignment.: The LWA demonstrates the capability to mitigate misalignment in Sec. III, offering a potential solution to address orbital perturbations in THz ISLs. Here, we quantify the tolerance under varying link geometries and evaluate the impact of dynamic beam pointing on data rates.

Setup. We assume a constant communication distance between two satellites, with their formation flying causing variations

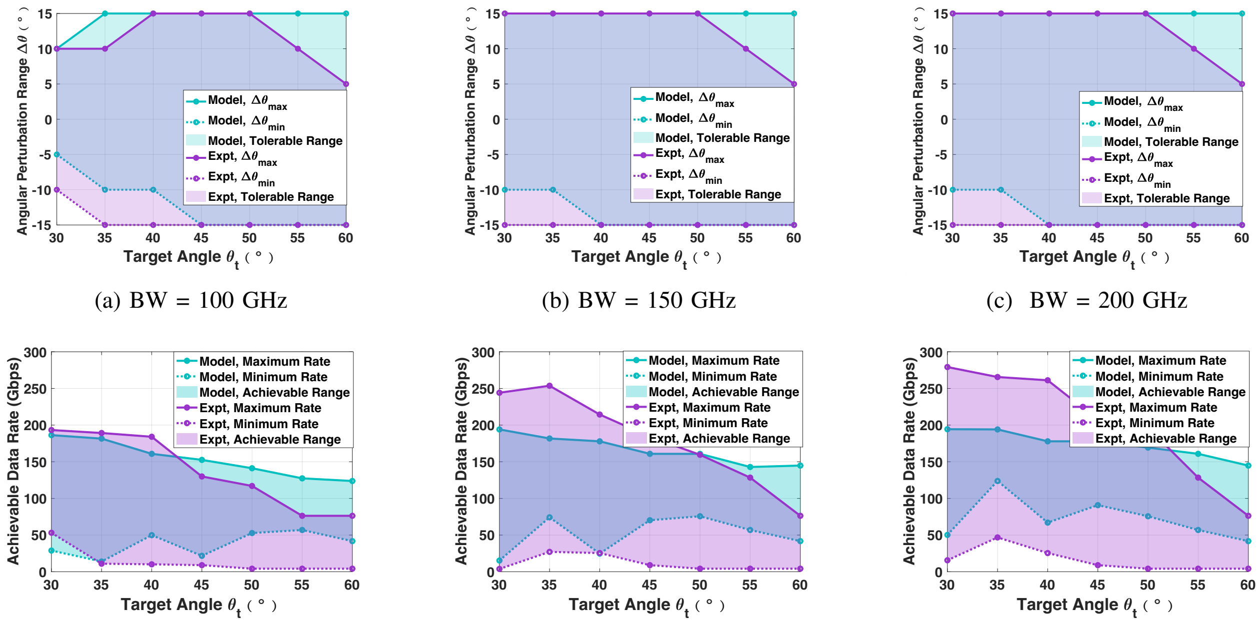

(a) BW = 100 GHz (b) BW = 150 GHz (c) BW = 200 GHz

(d) BW = 100 GHz (e) BW = 150 GHz (f) BW = 200 GHz

Fig. 8: Comparison of experimental and model-based tolerance to perturbations (a-d) and achievable aggregate rates within the tolerated range under varying bandwidths (e-h).

in relative angles. The target satellite is positioned at various angles to ensure initial alignment with the chaser, with θ_t limited to $[30°, 60°]$ in 5° steps. When orbital perturbations occur, the emission angle varies by $\Delta\theta$, simulating misalignment by adjusting the target's orientation within $[-15°, 15°]$. In this example, the total bandwidth of 100 GHz is divided into 32 subchannels (3.125 GHz each). We define a minimum threshold, SNR_{min}, representing the target satellite's sensitivity. A signal is detectable if any subchannel's SNR exceeds SNR_{min}. The corresponding $\Delta\theta$ is considered tolerated, while perturbations with all subchannels below SNR_{min} are intolerable. For each θ_t, we calculate the maximum and minimum tolerated $\Delta\theta$ ($\Delta\theta_{max}$ and $\Delta\theta_{min}$) to define the system's tolerance to orbital perturbations. Data rates are computed across the available bandwidth using Eqn. (7), with the maximum and minimum data rates defining the achievable range for the link.

Results. Figures 8a and 8d compare the experimental and model tolerance and data rates for varying θ_t under a 100 GHz bandwidth. In Fig. 8a, each θ_t exhibits different tolerance levels due to the angle-dependent transmission of the LWA-based ISL. For positive perturbations ($\Delta\theta > 0°$) resulting in higher emission angles, the experimental link shows lower tolerance than the model, especially for $30° < \theta_t < 40°$, due to differences in how the spectral peak shifts in the bandwidth, affecting θ coverage. At $\theta_t > 50°$, lower experimental SNR causes further discrepancy, as shown in Fig. 7. Conversely, for negative perturbations ($\Delta\theta < 0°$), the experiment shows higher tolerance. Prior studies estimate beam misalignment due to orbital perturbation at approximately 11° [9]. The link accommodates misalignments of $[-10°, 10°]$ for $30° < \theta_t < 55°$, ensuring reliable communication.

Figure 8d shows a consistent decline in data rates as θ_t increases in both the model and experiment due to narrower bandwidth at higher angles. Yet, experimental rates are lower than the model at higher angles due to reduced SNR, while at lower angles, the experiment shows slightly higher rates from a flatter SNR distribution, as discussed in Sec. IV-B. The large variation of nearly 150 Gbps between maximum and minimum rates highlights the impact of dynamic pointing on performance, with minimum rates nearing 0 Gbps under severe perturbations, which can degrade signal quality to near-zero data rates, despite signal detectability at the target.

2) Tolerance Enhancement: Thus far, we focus on the analysis of the perturbation tolerance within the bandwidth of 100 GHz. In LWA-based THz ISLs, the frequency-angle coupling implies that a wider bandwidth corresponds to an expanded spatial-signal footprint, thereby, enhancing the link's tolerance through broader coverage of θ. Here, we use a setup similar to Sec. IV-C1 and widen the bandwidth from 100 GHz to 200 GHz to evaluate the potential improvement in tolerance to orbital perturbations.

Results. The results in Fig. 8a, Fig. 8b, and Fig. 8c illustrate the enhancement of tolerance, while Fig. 8d, Fig. 8e, and Fig. 8f shows the data rate improvement in the tolerated perturbation range as the bandwidth increases from 100 GHz to 200 GHz.

As the bandwidth increases from 100 GHz to 150 GHz, both the model and experiment show improved tolerance, as indicated by the expanded purple and green regions in Fig.

8b, allowing a broader range of θ_t to tolerate perturbations within $[-10°, 10°]$, and extending to $[-15°, 15°]$ for most θ_t. This suggests wider bandwidth improves resilience to dynamic perturbations, enhancing communication reliability. However, both model and experiment still show intolerance in certain θ_t ranges—below $40°$ in the model and above $50°$ in the experiment, due to peak SNR dropping below SNR_{min} at higher angles in the experiment and underestimated power at lower angles resulting in undetectable signals (Sec. IV-B). Expanding bandwidth to 200 GHz (Fig. 8c) does not further increase $\Delta\theta$ coverage, demonstrating that tolerance does not scale proportionally with bandwidth, and misalignment cannot be fully mitigated. While additional bandwidth does not improve tolerance, it significantly increases data rates. Expanding from 100 GHz to 150 GHz adds 50 Gbps to the achievable rates, though the minimum rate shows little improvement. Similarly, increasing to 200 GHz further boosts achievable rates, highlighting the benefit of bandwidth expansion for throughput, provided sufficient spectral resources are available.

D. Optimal Geometry of LWA

The performance of the LWA-based link is influenced by the radiation pattern of LWA. In Sec. III, we introduce key parameters, such as the attenuation coefficient, α, and plate separation, b. Here, we study these parameters to guide the optimization of LWA geometry, aiming to enhance tolerance and data rates.

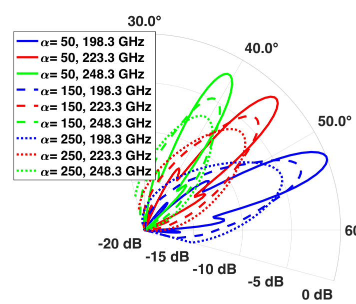

(a)

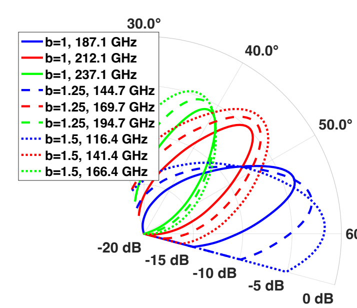

(b)

Fig. 9: Analysis of geometry of LWA through (a)varying attenuation coefficient α and (b) varying plate separation b

Setup. We use a setup similar to Sec. IV-C, with a 3.125 GHz subchannel bandwidth and center frequency based on the target satellite's spectral peak at $45°$, totaling 16 subchannels over 50 GHz. To study the effect of the attenuation coefficient α, we fix $b = 1mm$ and $L = 3cm$, varying α from 50 to 200 rad/m in 100 rad/m steps. Additionally, to assess plate separation b, we fix $\alpha = 200\ rad/m$ and $L = 3cm$, adjusting b from 1 to 1.5 mm in 0.25 mm increments.

Results. Figure 9a shows how the radiation pattern changes with increasing attenuation coefficient. For $\alpha = 50\ rad/m$, the beam becomes more directional with higher radiated power, improving antenna gain. While typically undesirable due to their lower power, the presence of sidelobes marginally enhances coverage and tolerance. Conversely, a higher α extends θ coverage, improving misalignment tolerance but reducing radiated power. Figure 9b shows that increasing plate separation b widens the beam and increases radiated power, improving efficiency. However, as b increases, the bandwidth shifts to lower frequencies, limiting radiation efficiency at higher angles. For $b = 1.5\ mm$, both the center frequency and the lower frequencies fall below 0.15 THz, which limits the LWA's ability to radiate efficiently at higher angles. Thus, optimizing b can improve tolerance and data rate, the LWA design must carefully account for the reduced angular range within the usable bandwidth to avoid performance trade-offs at higher frequencies.

V. Related Work

THz Communication for Inter-Satellite Links. THz frequencies, primarily used for passive sensing such as studying solar and astronomical activities [9], have shown potential for satellite communications [19], [20], with data rates up to 2.5 Gbps over 100 km [21]. Unlike optical laser-based ISLs, which struggle with beam alignment due to spacecraft jitter [3], or congested RF bands like UHF [2], our work highlights composite multi-channel THz links as a strong candidate for future ISLs by using custom THz-scale LWAs to provide higher tolerance to orbital misalignment.

THz Antenna Technologies for Space Applications. Prior studies have shown that THz metasurfaces [22], [23] and THz reconfigurable antennas [24], [25] can achieve high gain and narrow beam widths, which are essential for long-distance communication in space. In this paper, we explore adaptable LWAs for THz ISLs, which offer flexible, wideband beam steering without mechanical movement.

Orbital Dynamics and Satellite Constellation Management. Current pointing, acquisition, and tracking (PAT) solutions, such as CubeSat Infrared CrosslinK (CLICK) [3] and NASA's TeraByte InfraRed Delivery (TBIRD) [26], focus on LEO satellites and ground segment of the satellite network, causing beam divergence and lacking robustness for deep-space scenarios with more complex perturbations [27]. In contrast, this work offers wideband steerability and greater misalignment tolerance, ideal for managing dynamic perturbations in deep-space and multi-satellite constellations.

VI. Discussion and Future Work

Here we discuss further implications of THz ISLs and potential applications, and outline our plans for continuing this work.

Extending Coverage & Scaling to Concurrent ISLs. To improve coverage and adaptability, we are looking into *Multi-Face* LWAs, which integrate multiple angularly separated LWAs on different satellite faces, and *Multi-Slit* LWAs [7], [28] featuring multiple slots along the antenna for simultaneous radiation at various frequencies and angles, enabling wide angular radiation to compensate for misalignment due to satellite perturbations and supporting communication with multiple targets. To enable simultaneous communication between multiple satellites in large constellations, we propose that with the THz frequency diversity and the angular dispersion of LWAs, multiple links between multiple satellites in large constellations can be supported simultaneously, with different frequency bands allocated to each ISL, reducing interference and preserving high bandwidth [5], [6], [29].

Reconfigurable Intelligent Surfaces (RIS). The integration of RIS with THz ISLs is gaining interest [24], [30]. We propose RIS-assisted LWAs for enhanced beamforming precision [31]. Unlike conventional LWAs that rely on frequency-dependent steering, RIS adjusts the phase and amplitude of reflected THz waves in real-time, adapting to changes in satellite orientation without altering the signal frequency, and maintaining alignment despite perturbations.

Experimental Evaluations. Most research above 100 GHz has focused on short-range measurements, typically under 10 m, in urban and indoor line-of-sight scenarios due to challenges in achieving sufficient transmit power [13], [14], which significantly differ from operational ISL environments. to simulate satellite communication, we plan to conduct rooftop surrogate satellite/tower base station measurements at sub-THz frequencies [32], to validate LWAs' ability to isolate terrestrial and satellite networks, ensuring stable THz ISLs.

VII. Conclusion

This study demonstrates the efficacy of LWA in misalignment mitigation, which is crucial for adapting to orbital dynamics in THz ISL systems. We quantify the misalignment tolerance of varying link geometries and present the impact of bandwidth expansion on tolerance. We analyze the geometry of LWAs to guide the optimization of stable and high-quality communication links. Our findings are supported by theoretical analysis and preliminary experimental results, providing insights into designing reliable THz ISLs.

References

[1] I. F. Akyildiz and A. Kak, "The internet of space things/cubesats," *IEEE Network*, vol. 33, no. 5, pp. 212–218, 2019.

[2] R. Radhakrishnan *et al.*, "Survey of inter-satellite communication for small satellite systems: Physical layer to network layer view," *IEEE Communications Surveys & Tutorials*, vol. 18, no. 4, pp. 2442–2473, 2016.

[3] P. Grenfell, A. Aguilar, K. Cahoy, and M. Long, "Pointing, acquisition, and tracking for small satellite laser communications," 2018.

[4] N. J. Karl *et al.*, "Frequency-division multiplexing in the terahertz range using a leaky-wave antenna," *Nature Photonics*, vol. 9, no. 11, pp. 717–720, 2015.

[5] K. P. Dasala and E. W. Knightly, "Multi-user terahertz wlans with angularly dispersive links," in *Proceedings of the ACM MobiHoc*, 2022, pp. 121–130.

[6] K. Dasala and E. W. Knightly, "Scalable multi-user terahertz wireless networks with angularly dispersive links," *IEEE Transactions on Networking*, pp. 1–16, 2024.

[7] H. Guerboukha *et al.*, "Efficient leaky-wave antennas at terahertz frequencies generating highly directional beams," *Applied Physics Letters*, vol. 117, no. 26, 2020.

[8] A. Sutinjo, M. Okoniewski, and R. H. Johnston, "Radiation from fast and slow traveling waves," *IEEE Antennas and Propagation Magazine*, vol. 50, no. 4, pp. 175–181, 2008.

[9] S. Nie and I. F. Akyildiz, "Channel modeling and analysis of inter-small-satellite links in terahertz band space networks," *IEEE Trans. on Communications*, vol. 69, no. 12, pp. 8585–8599, 2021.

[10] M. N. Sweeting, "Modern small satellites-changing the economics of space," *Proceedings of the IEEE*, vol. 106, no. 3, pp. 343–361, 2018.

[11] W. Clohessy and R. Wiltshire, "Terminal guidance system for satellite rendezvous," *Journal of the aerospace sciences*, vol. 27, no. 9, pp. 653–658, 1960.

[12] A. H. De Ruiter, C. Damaren, and J. R. Forbes, *Spacecraft dynamics and control: an introduction*. John Wiley & Sons, 2012.

[13] T. S. Rappaport *et al.*, "Wireless communications and applications above 100 ghz: Opportunities and challenges for 6g and beyond," *IEEE access*, vol. 7, pp. 78 729–78 757, 2019.

[14] S. Koenig, *et al.*, "Wireless sub-thz communication system with high data rate," *Nature photonics*, vol. 7, no. 12, pp. 977–981, 2013.

[15] D. R. Jackson, A. A. Oliner, and C. Balanis, "Modern antenna handbook," in *Leaky-Wave Antennas*. Wiley, 2008, pp. 345–366.

[16] Y. Ghasempour *et al.*, "Single-shot link discovery for terahertz wireless networks," *Nature communications*, vol. 11, no. 1, pp. 1–6, 2020.

[17] ——, "Leakytrack: non-coherent single-antenna nodal and environmental mobility tracking with a leaky-wave antenna," in *Proceedings of the Sensys*, 2020, pp. 56–68.

[18] I. Duling and D. Zimdars, "Revealing hidden defects," *Nature Photonics*, vol. 3, no. 11, pp. 630–632, 2009.

[19] S.-W. Dong *et al.*, "Advances of terahertz research and terahertz satellite communications," in *2011 ICECC*. IEEE, 2011, pp. 4122–4125.

[20] T. Nagatsuma and A. Kasamatsu, "Terahertz communications for space applications," in *2018 APMC*. IEEE, 2018, pp. 73–75.

[21] Y.-M. Ding, S. Gao, X. Shi, and H. Wu, "Analysis of inter-satellite terahertz communication link," in *WCSN 2016*. Atlantis Press, 2016, pp. 180–183.

[22] X. Zang *et al.*, "Metasurfaces for manipulating terahertz waves," *Light: Advanced Manufacturing*, vol. 2, no. 2, pp. 148–172, 2021.

[23] K. W. Cho *et al.*, "Towards dual-band reconfigurable metasurfaces for satellite networking," in *Proc. of the ACM HotNets*, 2022, pp. 17–23.

[24] K. Tekbiyik, G. K. Kurt, A. R. Ektı, and H. Yanikomeroglu, "Reconfigurable intelligent surfaces empowered thz communication in leo satellite networks," *IEEE Access*, vol. 10, pp. 121 957–121 969, 2022.

[25] H. Du *et al.*, "Performance and optimization of reconfigurable intelligent surface aided thz communications," *IEEE Trans. on Communications*, vol. 70, no. 5, pp. 3575–3593, 2022.

[26] J. Chang *et al.*, "Body pointing, acquisition and tracking for small satellite laser communication," in *SPIE Free-Space Laser Communications XXXI*, vol. 10910, 2019, pp. 144–152.

[27] A. J. Swank, E. Aretskin-Hariton, D. K. Le, O. Sands, and A. Wroblewski, "Beaconless pointing for deep-space optical communication," in *34th AIAA International Communications Satellite Systems Conference*, 2016, p. 5708.

[28] A. Kludze *et al.*, "Quasi-optical 3d localization using asymmetric signatures above 100 ghz," in *Proceedings of the ACM MobiCom*, 2022, pp. 120–132.

[29] S. Saha and K. Dasala, "Terahertz inter-small-satellite communications via angularly dispersive antennas," in *2024 49th IRMMW-THz*, 2024, pp. 1–2.

[30] S.-W. Qu *et al.*, "Terahertz reflecting and transmitting metasurfaces," *Proceedings of the IEEE*, vol. 105, no. 6, pp. 1166–1184, 2017.

[31] Y. Chen, J. Tan, M. Hao, R. MacKenzie, and L. Dai, "Accurate beam training for ris-assisted wideband terahertz communication," *IEEE Trans. on Communications*, 2023.

[32] Y. Xing and T. S. Rappaport, "Terahertz wireless communications: Co-sharing for terrestrial and satellite systems above 100 ghz," *IEEE communications letters*, vol. 25, no. 10, pp. 3156–3160, 2021.